



Tool-pin profile effects on thermal and material flow in friction stir butt welding of AA2219-T87 plates: computational fluid dynamics model development and study

Ramana Murthy Bagadi¹ · Jeevan Jaidi¹ · Atmakur Venugopal Rao² · Suresh Dadulal Meshram²

Received: 4 July 2023 / Accepted: 25 February 2024 / Published online: 5 March 2024
© The Author(s), under exclusive licence to Springer-Verlag London Ltd., part of Springer Nature 2024

Abstract

A three-dimensional coupled model in a Eulerian framework has been developed in COMSOL Multiphysics software and used to study the complex phenomena of thermal and material flow during the friction stir welding (FSW) process. The moving heat source (tool) effect is modelled using a coordinate transformation. The frictional heat as a function of temperature-dependent yield strength of AA2219-T87 material and the deformation energy of plasticized material flow are considered. Further, the plasticized material flow around the rotating tool is modelled as non-Newtonian fluid using partial-sticking/sliding boundary condition with a computed slip factor (δ) at the workpiece-tool material interfaces. The coupled Eulerian model prediction accuracy has been validated against the experimental weldment zones and found a good agreement in terms of the shape and size. Subsequently, the effects of tool-pin profiles (cylindrical and conical) on thermal distribution, material flow, shear strain rates, thermal histories, and weldment zones were studied. It is found that the maximum temperatures, material flow velocities, and shear strain rates are low with the conical tool pin in contrast to the cylindrical one, and it is partly attributed to increased mixing of shoulder and pin-driven material flow around the rotating tool, which in turn decreased the size of weldment zones. Also, the maximum temperatures, material flow velocities, and shear strain rates on the advancing side are higher than those of the retreating side. Therefore, it is suggested to use the CFD model to design the FSW process and tool parameters in a cost-effective way in contrast to the tedious experimental route.

Keywords FSW · CFD model · Weldment zones · Deformation energy · Shear strain rate

Nomenclature

AS	Advancing side	h_{conv}	Heat transfer coefficient ($\text{W}/\text{m}^2 \cdot \text{K}$)
CFD	Computational fluid dynamics	k	Thermal conductivity ($\text{W}/\text{m} \cdot \text{K}$)
C_p	Specific heat ($\text{J}/\text{kg} \cdot \text{K}$)	MUMPS	Multifrontal massively parallel sparse
DSC	Differential scanning calorimetry	p	Pressure (Pa)
D, d	Shoulder diameter, pin diameter	PARDISO	Parallel Sparse Direct Solver
F	Volume force source term (N/m^3)	q	Heat flux (W/m^2)
FE	Finite element	Q_{vd}	Viscous dissipation energy (W/m^3)
FSW	Friction stir welding	r	Radius (mm)
HAZ	Heat-affected zone	RS	Retreating side; rotational speed (rpm)
H	Tool-pin height (mm)	SS	Stainless steel
		t	Time (s)
		T	Temperature (K)
		TMAZ	Thermomechanically affected zone
		TS	Traverse speed (mm/min)
		TWI	The Welding Institute
		T_m	Melting temperature (K)
		u	Velocity component (m/s)
		\mathbf{u}	Velocity vector (m/s)
		μ_{app}	Apparent viscosity ($\text{kg}/\text{m} \cdot \text{s}$)
		u_{trans}	Translational (traverse) speed (m/s)

✉ Jeevan Jaidi
jaidi@hyderabad.bits-pilani.ac.in

¹ Department of Mechanical Engineering, Birla Institute of Technology and Science-Pilani, Hyderabad Campus, Hyderabad, Telangana 500078, India

² Modelling and Simulation Group, Defence Metallurgical Research Lab (DMRL), Hyderabad, Telangana 500058, India

v	Velocity component (m/s)
WNZ	Weld nugget zone
x, y, z	Space coordinates (m)

Greek symbols

ρ	Density (kg/m^3)
ω	Angular velocity (rad/s)
δ	Slip factor
ΔT	Temperature difference (K)
σ_y	Yield strength (N/m^2)
$\dot{\gamma}$	Shear strain rate (1/s)
∇	Vector differential operator

Subscripts and superscripts

b	Bottom
m	Melting
p	Pin
s	Shoulder
t	Tool, top

1 Introduction

The age-hardened aluminium-alloy plates of AA2219-T87 are widely used in the fabrication of critical defence and aerospace components such as liquid cryogenic rocket motor shells and propulsion fuel tanks, because of its unique combination of properties (high strength to weight ratio, high fracture toughness, and excellent properties at cryogenic temperatures). However, the fabrication of components using conventional fusion welding techniques poses several challenges in achieving the integrity of welds due to issues such as solidification cracking, porosity, distortion, and high residual stresses. Friction stir welding (FSW), a solid-state joining technique developed in year 1991 by The Welding Institute (TWI), the UK [1], is an alternative to overcome the above-mentioned difficulties through the avoidance of melting and solidification and achieving high quality joints. The FSW process uses a non-consumable tool to weld two metal plates by the combined effect of frictional heat and mechanical forces, which soften and stir the workpiece material around the rotating tool. However, controlling the maximum temperatures to avoid the precipitate coarsening and dissolution as well as sufficient material flow around the tool critically depends on the selection of FSW process and tool parameters, including the tool-pin profile. The following paragraphs briefly discuss on the experimental and simulation works done on FSW butt joints of metal plates and the role of process and tool parameters to achieve the weld joint and quality.

Researchers have experimentally studied the effects of process parameters (tool speeds and load) and tool parameters (shoulder and pin diameters, pin profiles, tilt angle, pin without and with threads) on the weld geometry and joint strength of aluminium and steel alloy plates butt-welded

with friction stir welding (FSW) technique. Elangovan and Balasubramanian [2, 3] reported that the defect-free weld nugget zone (WNZ) depends largely on the tool-pin profile and traverse (welding) speed. Kumar and Kailas [4] interpreted that the formation of onion rings in stir zone (SZ) and defect-free welds is solely by the interaction of shoulder and tool-pin-driven material flow and mixing. Fratini et al. [5] used a marker tracer technique and observed the final position of marker particles. They reported that the conical tool pin overcomes the defects and also improves the mechanical properties over the cylindrical tool pin. Biswas and Mandal [6] performed experiments as well as thermal simulations with cylindrical and conical tool-pin profiles. They found through experiments that the tendency of wormhole defect increased with increasing the base diameter of tool-pin profiles. Ramanjaneyulu et al. [7, 8] found that the size of sheared and rotating layer in TMAZ reduced monotonically with the tool-pin profiles, in the sequence of triangular, conical, square, pentagon, and hexagon. Meshram et al. [9] found surface and tunnel defects with plain conical pin at rotational speeds over 1200 rpm, while sound welds with threaded conical pin at much low and high speeds (600–2400 rpm). Meshram and Reddy [10] observed surface defects with tilt angles less than 0.5° and internal defects with tilt angles above 2.5° .

Several researchers have numerically studied the effect of FSW process and tool parameters on thermal and material flow fields, thermal cycles, shear and plastic strain rates, and flow and residual stresses depending on different frameworks used, such as Eulerian, Lagrangian, and Arbitrary Lagrangian and Eulerian. Xu et al. [11] performed 2-D steady-state simulations in ALE framework and predicted the plasticized material flow around the tool pin. However, they used measured temperatures as input and no explicit modelling on heating generation was done. Schmidt et al. [12] predicted the heat generation at interfaces between workpiece-tool materials with different contacting conditions (sticking, sliding, partial sticking-sliding). The predicted results were compared with experimental data and found defect-free weld. Seidel and Reynolds [13, 14] used a 2-D model to study the material flow around the circular tool pin. Also, they experimented using marker tracers and observed that a vertical mixing occurred [13], particularly at low traverse and high rotational speeds. Chen and Kovacevic [15] used ANSYS software and modelled the thermomechanical phenomena. The heat generation was modelled using frictional contact at workpiece-tool interfaces. The authors found that longitudinal stresses are higher than the transverse ones near the weld crown and are increased with increasing traverse speed. However, the mechanical consolidation effects by the tool pin were ignored and also neglected the material flow deformation energy. Zhu and Chao [16] developed a 3-D thermal model without

considering the material flow. The authors calculated the heat at workpiece-tool interfaces through inverse analysis based on the measured temperatures at selected locations and found that about 50% of the energy is diffused into the stainless-steel (304L) workpieces in contrast to 75–80% in Al-alloy workpieces [17]. Zhang et al. [18] developed a 2-D FE model in ABAQUS and studied the material flow and residual stresses. The workpieces were considered isotropic behaviour with hardening effects along with von Mises yield criterion. They observed a non-uniform material flow around the tool pin. However, the measured temperatures were used as input and constructed the spatial temperature field. Nandan et al. [19, 20] performed 3-D simulations on the material flow in FSW of stainless-steel and aluminium-alloy plates with the cylindrical tool. They found that the forces and torque acting on the tool pin depend on process as well as tool parameters. However, the authors solved steady-state equations in Eulerian framework and did not consider the path-dependent material behaviour. Buffa et al. [21, 22] simulated the thermomechanical phenomena in DEFORM-3D software, and ALE approach with adaptive meshing was used to account for the large deformations. The predicted results were compared with the measured forces and temperatures and showed the asymmetry of zones. Khandkar et al. [23] discussed a 3-D FE analysis of thermomechanical behaviour. They used temperature field from thermal model as input to structural model, but the mechanical action by the tool pin was not accounted. Also, one width of the plates was used and neglected material flow deformation energy. Bastier et al. [24] simulated the 3-D steady-state thermomechanical effects in two stages; in the first step, only thermal effects were simulated in a Eulerian frame and in the second step, a steady-state algorithm based on an elasto-viscoplastic model to predict the residual stresses. They found the low temperatures and residual distortions at high welding speed and low rotational speed. However, constant thermal and mechanical properties were used.

Grujicic et al. [25–27] used a coupled Eulerian-Lagrangian approach for thermomechanical-material flow and considered the frictional and deformation heat energy. Also, the precipitates' behaviour (precipitate coarsening, over-aging, dissolution, and re-precipitation) in aluminium alloy, AA2xxx [26], was studied. Further, the effects of weld pitch, tool tilt angle, and the tool-pin size on the flow pattern and the extent of material mixing were investigated. The authors found that the longitudinal and transverse residual stresses increased with increasing rotational and travel speeds [25]. Mohanty et al. [28] numerically and experimentally investigated on the temperature distribution and material flow behaviour and found that they vary depending on the tool-pin profile (cylindrical and conical) and contact conditions at the workpiece-tool interfaces. Al-Badour et al. [29] developed a 3-D Coupled Eulerian and Lagrangian (CEL)-based

FE model in ABAQUS. They considered modified and classical forms of Coulomb's frictional law with different coefficients of friction (0.3, 0.58, 0.8) to analyze its effect on the weld defect formation. Hamilton et al. [30] developed thermal-material flow model in COMSOL software and predicted the material deformation around the tool. Further, the differential scanning calorimetry (DSC) thermal analysis data along with the model predictions were used to predict the onion ring pattern. Jain et al. [31] performed 3-D thermomechanical simulations and studied the effect of process parameters and tool-pin profiles (cylindrical and conical) in terms of the tool forces and torque, temperatures, and strain rates. They found that the plastic strain rates are higher on the advancing side as compared to the retreating side. However, no comparison was made with the measured and predicted weld zones vs. tool-pin profiles. Kadian and Biswas [32] performed thermal-material flow simulations in ANSYS CFD software and studied the effect of different tool-pin profiles on the material flow. They found that the difference in peak temperatures on advancing and retreating sides depends on the tool-pin profile. However, they did not show asymmetry in the weld zones. Sahlot et al. [33] developed a 3-D thermal model considering frictional heat, and the predicted temperatures were validated against the measured data. However, they did not consider the material flow in the simulations. Tiwari et al. [34] developed a thermal-material flow model in ANSYS CFD software and considered the workpieces as non-Newtonian fluid. The authors found a vortex region on the advancing side and related it to be a source of defect formation. Pandian and Kannan [35] performed 3-D simulations in COMSOL software using moving coordinate system for FSW process of dissimilar materials and considered the frictional heat generation and stick-slip boundary condition. However, the authors did not show the material flow around the tool pin. Vicharapu et al. [36] performed 3-D thermomechanical simulations for a stationary shoulder friction stir welding (SSFSW), primarily to reduce the heat generation and residual stresses. They found that the maximum longitudinal tensile stresses are around 30–45% of the yield strength of base metal (BM). However, the authors neglected the material flow around the tool. Kesharwani et al. [37] used 3-D thermal-material flow model in COMSOL software and investigated on the role of number of flat faces on the local heat generation and material flow. They found that four flat surfaces are more effective in thermal softening of workpiece material. Andrade et al. [38] used 3D thermomechanical model and validated the predicted temperatures and strain rates with experimental data by calculating the grain sizes in the stir zone using Zener-Hollomon parameter. A coupled 3-D thermal-material flow model using CFD approach was developed for the FSW process of AA2xxx plates [39–41]. The effect of process parameters on the net heat generation during different stages

of the FSW process was predicted by Shi and Wu [40]. The authors predicted the tool torque and compared it with the measured data. However, they did not show the weldment zones. Su et al. [39] performed simulations with different tool-pin profiles (conical and triangular surfaces) and contact conditions (fully sliding, fully sticking, and partial sticking/sliding) and studied the effect of process parameters on temperature distribution and plasticized material flow. The authors compared the predicted thermal cycles with the measured data. However, the predicted weldment zones were not compared with the experiments. Chen et al. [41] studied the effect of conical tool-pin dimensions on thermal and material flow behaviour and the resulting shape and size of weldment zones. The authors found that the tool-pin dimensions have significant influence on the size of TMAZ at its centre, but not at the top and bottom.

It can be noted from the above literature summary on FSW process simulations that a couple of research groups have attempted to predict the plasticized workpiece material flow around the rotating tool using a tangential boundary condition with a varied slip factor (δ) between the rigid tool and workpiece materials [39]. However, they did not show the plasticized material flow with mixing pattern and the resulting individual weld zones (WNZ, TMAZ, and HAZ) in the cross-section using representative isotherms. In the present simulations, a partial-sticking/sliding boundary condition with computed slip factor (δ) at the workpiece-tool material interfaces and around the rotating tool is used. Further, the effect of tool-pin profiles (cylindrical and conical) on the resulting material flow and mixing, the heat distribution around the tool, the size and shape of weld zones, and the shear strain rate variation are studied during the friction stir butt welding of AA2219-T87 plates at high traverse (welding) speed.

2 Mathematical and numerical modelling

In this section, the governing equations, the geometry (computational domain) and mesh, the initial and boundary conditions, the thermophysical property data of workpieces (aluminium alloy, AA2219-T87) and tool (structural steel) materials, and the numerical techniques used in COMSOL Multiphysics software are briefly discussed.

2.1 Mathematical modelling

The governing equations pertaining to the heat transfer in solids and fluids used in COMSOL Multiphysics software along with the auxiliary equations for heat flux input and contact boundary conditions used are discussed below.

2.1.1 Heat transfer in solid

In friction stir welding (FSW) process, the heat generation by friction between workpiece and tool materials at shoulder and pin surfaces is given as heat flux input boundary condition. Also, the moving heat source (tool) effect is modelled using a coordinate transformation between workpiece and tool as discussed by Jaidi and Dutta [42] and hence, an additional term in the governing equations is introduced and assumed workpiece and tool are fixed (i.e. fully Eulerian framework). Therefore, the governing transient heat conduction (diffusion) equation for the workpieces and tool is given by

$$\rho C_p \frac{\partial T}{\partial t} + \rho C_p \mathbf{u}_{\text{trans}} \cdot \nabla T = -\nabla \cdot \mathbf{q} \quad (1)$$

where ρ and C_p are density and specific heat of a material, respectively; \mathbf{q} is conduction heat flux rate within the material; and $\mathbf{u}_{\text{trans}}$ is velocity vector of translational motion (i.e. welding speed) of heat source.

2.1.2 Heat transfer in solid and fluid

Due to heating and shearing of workpieces by the rotating tool, the plasticized material deforms and flows around the tool. Therefore, convection heat transfer within the workpieces is governed by the mass, momentum, and energy equations with a source term for the moving heat source effect which are given below [43].

Continuity:

$$\rho \nabla \cdot \mathbf{u} = 0 \quad (2)$$

Momentum:

$$\rho \frac{\partial \mathbf{u}}{\partial t} + \rho (\mathbf{u} \cdot \nabla) \mathbf{u} = \nabla \cdot [-p\mathbf{I} + \mathbf{K}] + \mathbf{F} \quad (3)$$

where $\mathbf{K} = \mu_{\text{app}} (\nabla \mathbf{u} + (\nabla \mathbf{u})^T)$, $\mathbf{F} = -\frac{\partial}{\partial x} (\rho u_{\text{trans}} \mathbf{u})$, and μ_{app} is apparent viscosity.

Energy:

$$\rho C_p \frac{\partial T}{\partial t} + \rho C_p \mathbf{u} \cdot \nabla T = -\nabla \cdot \mathbf{q} + Q_{\text{vd}} \quad (4)$$

where Q_{vd} is volumetric heat generation rate by the viscous dissipation of plasticized material flow.

2.1.3 Initial and boundary conditions

It is assumed that the workpieces are deforming and tool is rigid, and both are initially at room temperature. Also, all the vertical surfaces of workpieces and tool are subjected to heat loss by convection ($h_{\text{conv}} = 25 \text{ W/m}^2 \cdot \text{K}$) during the FSW process. The heat loss from the bottom surface

of the workpieces is considered with a higher convection ($h_{conv} = 100\text{W/m}^2 \cdot \text{K}$). Further, the tangential velocity boundary conditions using partial sticking/sliding with a slip factor (δ) at the tool-workpiece material interfaces (shoulder and pin surfaces) are given by the following (Schmidt et al. [44]):

$$u = -\delta y \omega \tag{5}$$

$$v = \delta x \omega \tag{6}$$

where ω is angular velocity of the tool, and (x, y) are coordinates of interfaces from the tool axis. It can be noted that the cylindrical and conical pin surfaces across the tool-pin height are different and are represented by a coordinate variable, ' $r(x, y)$ ' - a radial distance from the tool axis. Therefore, the tangential flow boundary condition at the workpiece-tool material interfaces (Eqs. (5) and (6)) has the variables ' r ' and slip factor (δ). The later variable is non-uniform around the tool and it is computed from the predicted material flow field and used during the iterative solution.

2.1.4 Frictional heat generation

The heat generation by friction at the tool-workpiece material interfaces is treated as heat flux boundary condition (Bachmann et al. [45]):

$$\dot{q}^e(r) = \frac{r\omega\sigma_y(T)}{\sqrt{3}} \tag{7}$$

where σ_y is workpiece material yield strength.

2.1.5 Apparent viscosity

The non-Newtonian flow behaviour of the plasticized workpiece material is treated as a function of temperature-dependent yield strength and shear strain rate and it is given by the following discussed by (Colegrove and Shercliff [46]):

$$\mu_{app}(T, \dot{\gamma}) = \frac{\sigma_y(T)}{\sqrt{3} \dot{\gamma}} \tag{8}$$

2.2 Geometry, mesh, and material data

A butt joint of aluminium-alloy plates with two different tool-pin profiles (cylindrical and conical) is considered for the FSW process simulations. Table 1 gives the dimensions of workpiece(s) and tool-pin profiles. Figure 1 shows the computational domain (workpieces and tool). It can be noted that the individual workpieces are split for the purpose of meshing with a fine mesh around the rotating tool and coarse mesh away from it, as shown in Fig. 2. Also, the tool (rigid

Table 1 Workpiece and tool dimensions used in present simulations

Work-piece (mm)	Tool-pin profile	Tool-shoulder dia., d_s (mm)	Tool-pin top dia., $d_{p,t}$ (mm)	Tool-pin bottom dia., $d_{p,b}$ (mm)	Tool-pin height, h_p (mm)
300 × 75 × 6	Cylindrical	21	8	-	5.5
	Conical	21	8	5.5	

body) is meshed with tetrahedral elements to keep the number of elements low and to find out the maximum temperature the tool gets heated during the FSW process. A total of 0.28 million mesh elements with a minimum and maximum element size of 0.5 mm and 1 mm, respectively, is used in the present simulations. The thermophysical and mechanical properties of workpiece material (AA2219-T87) are given in Tables 2 and 3. The tool material is structural steel (SS), whose thermophysical properties available in COMSOL software data base (7850 kg/m³, 44.5 W/m·K, and 475 J/kg·K) are used.

2.3 Numerical techniques

COMSOL Multiphysics is a finite element (FE)-based commercial software with interfacing option of several physics modules available, which in principle helps to study the role of individual phenomena in a complex system, such as the friction stir welding (FSW) process—a fully coupled thermomechanical-material flow with metallurgical effects. In the present numerical study, a coupled thermal-material flow model is developed to study the role of tool-pin profiles on plasticized material flow with deformation energy generation (viscous dissipation effect), which influences the weld quality. The convergence of a transient simulation depends on selection of solver type and time-step size, which are briefly discussed below.

2.3.1 Solver type

COMSOL software offers a range of solvers, and therefore, it is important to choose the one that is best suited for the problem under consideration. In general, direct and iterative solvers are used for the transient analysis. Direct solvers (PARDISO and MUMPS) are more accurate but slower than iterative solvers (GMRES, FGMRES, and BiCGStab). In the present simulations, PARDISO for heat transfer in solids and MUMPS for heat transfer in fluids are used.

2.3.2 Time-step

The time-step size must be carefully selected based on the type of equations to be solved. A fixed time-step of 0.025 s is used in the present simulations, performed for a maximum of 60

Fig. 1 Computational domain: **a** workpieces and tool; **b** cylindrical tool-pin profile; **c** conical tool-pin profile

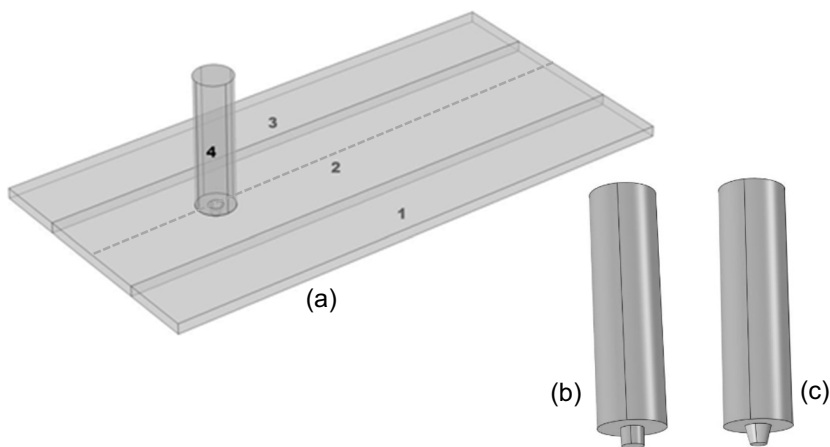


Fig. 2 Meshed computational domains: **a** workpieces with tool fixed at the weld centre line; **b** exploded view of mesh around tool; **c** exploded view of mesh in thickness direction and along weld centre line

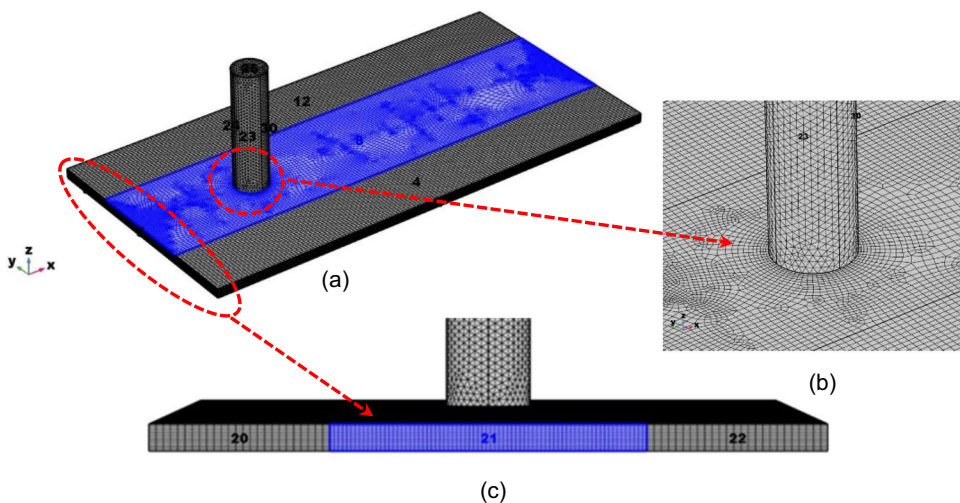


Table 2 Thermophysical properties of workpiece (AA2219-T87) [47]

Temperature, T (K)	298.15	373.15	473.15	573.15	673.15	773.15
Thermal conductivity, k (W/m•K)	130	142	151	159	172	185
Specific heat, C_p (J/kg•K)	864	887	921	921	963	1000

Table 3 Yield strength of workpiece (AA2219-T87) [18]

Temperature, T (K)	298	373	475	533	589	644	700	755
Yield strength, σ_y (MPa)	278.12	260.68	221.01	152.26	73.87	36.84	21.58	10.49

son on a Dell Workstation (256 GB RAM and 32 cores). Each simulation took a computer time of 15–16 h.

3 Results and discussion

3.1 Validation of coupled Eulerian model

The present Eulerian-based coupled thermal-material flow model prediction accuracy has been tested by comparing the predicted weldment zones (Weld Nugget Zone (WNZ), $T >$

603 K; thermomechanically affected zone (TMAZ), 570 K $< T \leq 603$ K; heat-affected zone (HAZ), 457 K $< T \leq 570$ K) with the measured zones by Manikandan et al. [48]. It must be noted that the above temperature ranges for different zones of AA2219-T87 material are inferred from the literature on precipitation kinetics study by Kang et al. [49] as well as the measured temperatures in different zones by Manikandan et al. [48]. In this validation exercise, a friction stir butt welding of AA2219-T87 plates (300 mm \times 200 mm \times 6 mm) by a conical tool pin (H13 tool steel) with a shoulder diameter of 23.8 mm, pin top diameter of 9 mm,

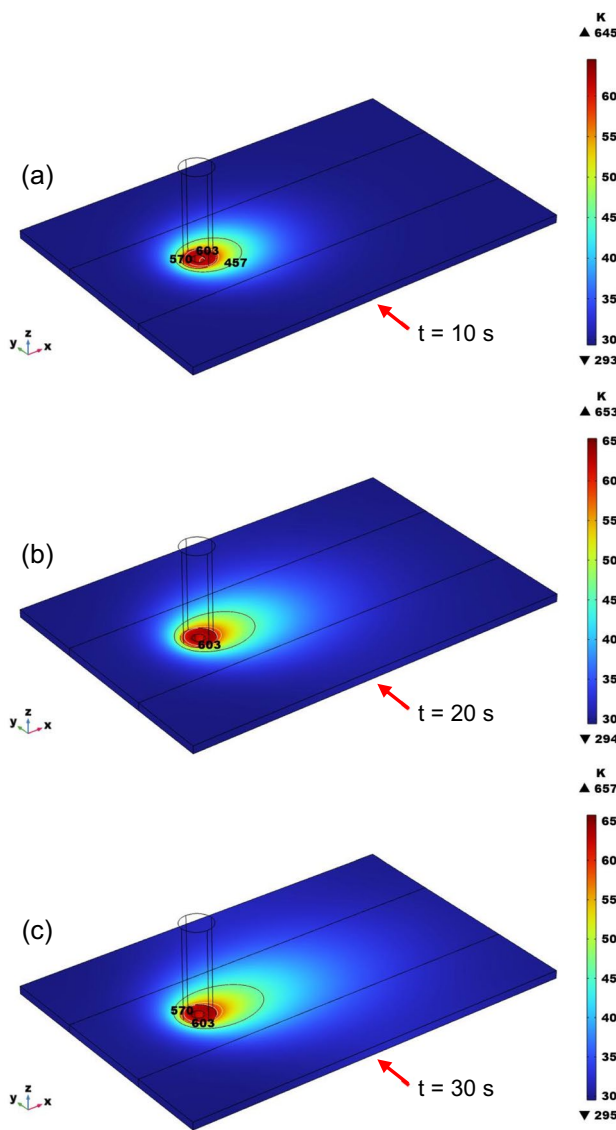


Fig. 3 Evolution of thermal field around moving heat source (conical tool pin) during FSW process at 400 rpm and 250 mm/min

pin bottom diameter of 6.8 mm, and pin height of 5.8 mm is considered [48]. The process parameters used are tool rotational speed (400 rpm) and traverse speed (250 mm/min).

Fig. 4 Comparison of predicted and measured weldment zones with a conical tool pin at 400 rpm and 250 mm/min: **a** measured; **b** predicted

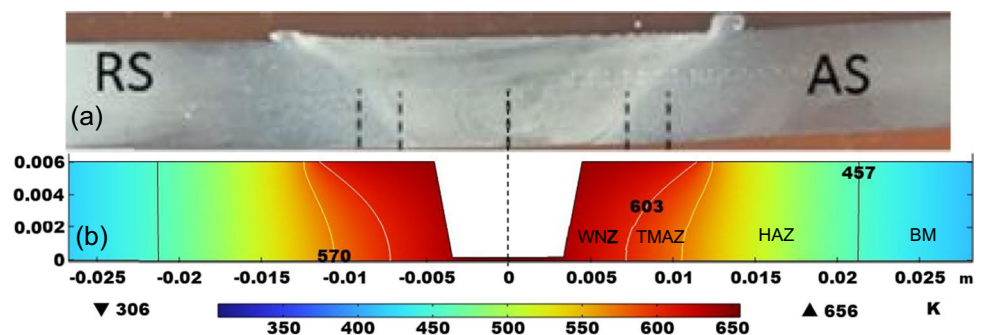


Figure 3 shows the evolution of temperatures within the workpieces due to moving heat source (conical tool pin) in Eulerian (fixed) coordinate system. The net heat generation considered is due to the friction between tool and workpiece materials and the deformation energy of plasticized material flow around the rotating tool. The moving heat source effects are considered using a source term in the momentum and energy equations [42] keeping tool and workpieces fixed (as seen in Fig. 3). The advantage of using fully Eulerian framework is to avoid the workpiece edge effect as well as the re-meshing of workpieces, which will minimize the computational time and storage space requirements. It is clearly observed in Fig 3 that with increasing the simulation time, the temperatures increased everywhere within the workpieces. However, the increase in maximum temperature after 30 s is negligibly small, and hence, the results after 60 s are considered steady state and used for subsequent discussion.

Figure 4 depicts the comparison between predicted and measured weldment zones [48]. It can be clearly observed that the size and shape of different zones at top and bottom of the plates are in close agreement, which indicates the precise modelling of plasticized workpiece material flow around the tool-pin profile by the present coupled thermal-material flow model. Further, a noticeable asymmetry of WNZ and TMAZ on advancing and retreating sides, with a flat shape and increased size on retreating side in contrast to advancing side, is in agreement with the general observation from the experiments. Table 4 compares the predicted and measured widths of different weld zones at the middle of weldment. Due to the tool rotation effect, more amount of plasticized material flows on the advancing side and results in more heat dissipation which in turn increases the width in contrast to the retreating side. The present coupled model predicted result clearly shows the trend and it is in agreement with the measured data. Also, the relative percentage error between the predicted and measured widths of different zones, both on advancing and retreating sides, is less than 6% and it is attributed to the non-consideration of mechanical effects in the present coupled thermal-material flow model (i.e. CFD approach). It must be noted that the potential influence by the deformation of workpieces cannot be accounted through

Table 4 Predicted vs. measured widths of weld zones at the middle of weldment

Weld zone	Measured width (mm)		Predicted width (mm)		Relative error (%)	
	Adv. side	Ret. side	Adv. side	Ret. side	Adv. side	Ret. side
Weld nugget zone (WNZ)	7.0	6.7	7.3	7.0	4.2	4.47
Thermomechanically affected zone (TMAZ)	9.9	9.5	10.4	10.0	5.05	5.26
Heat-affected zone (HAZ)	22.0	22.0	21.75	21.50	1.13	2.38

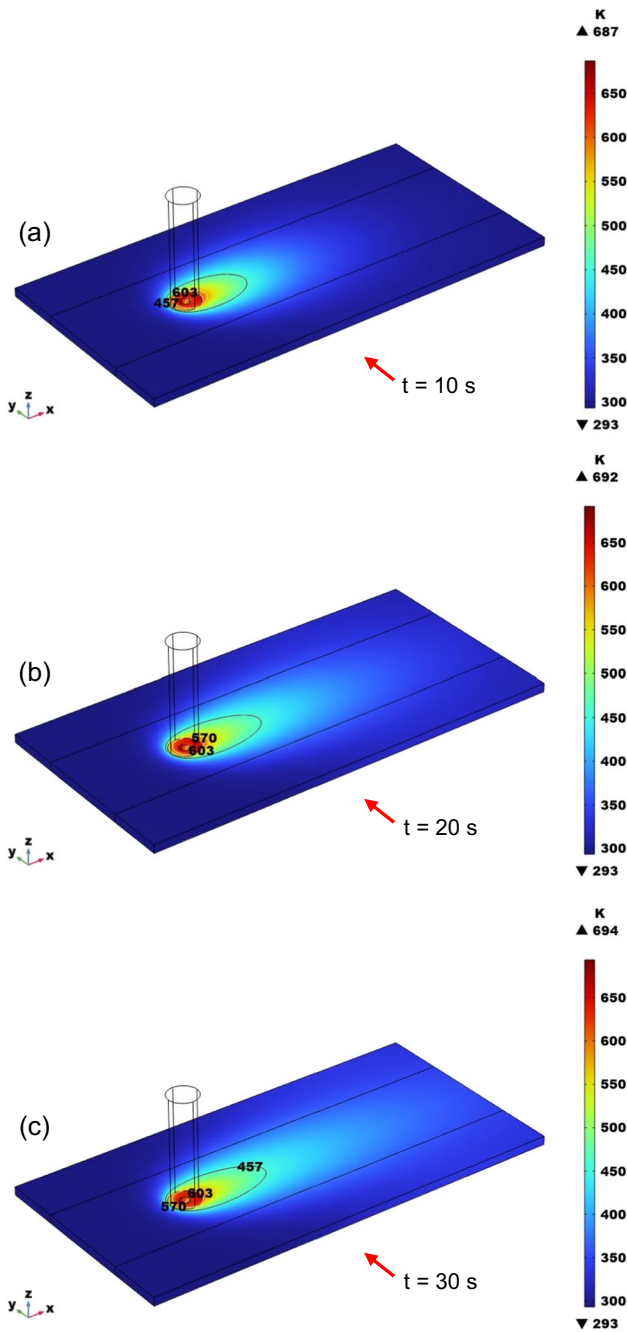


Fig. 5 Evolution of thermal field around moving heat source (cylindrical tool pin) during FSW process

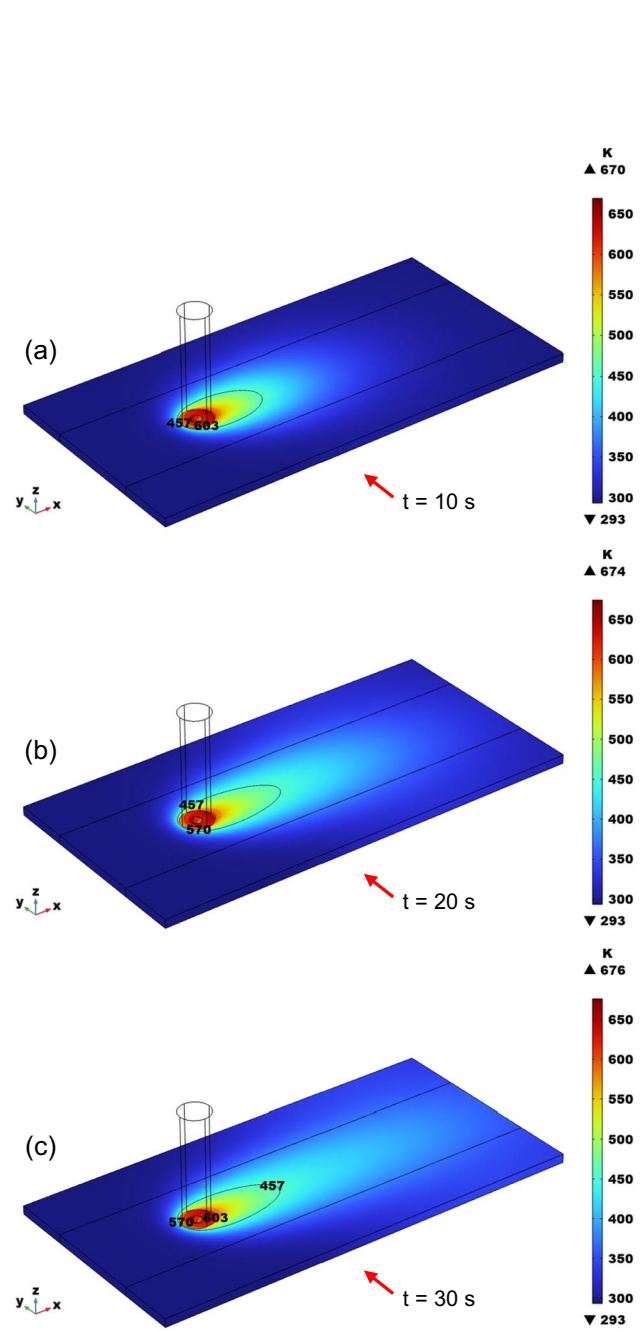


Fig. 6 Evolution of thermal field around moving heat source (conical tool pin) during FSW process

Fig. 7 Temperature distribution in workpiece and tool materials, sectioned along the weld axis: **a** with cylindrical tool pin; **b** with conical tool pin

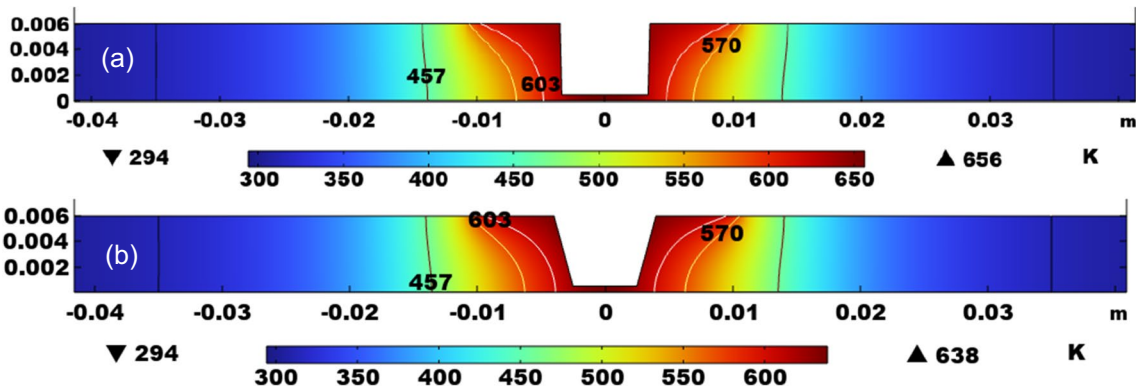
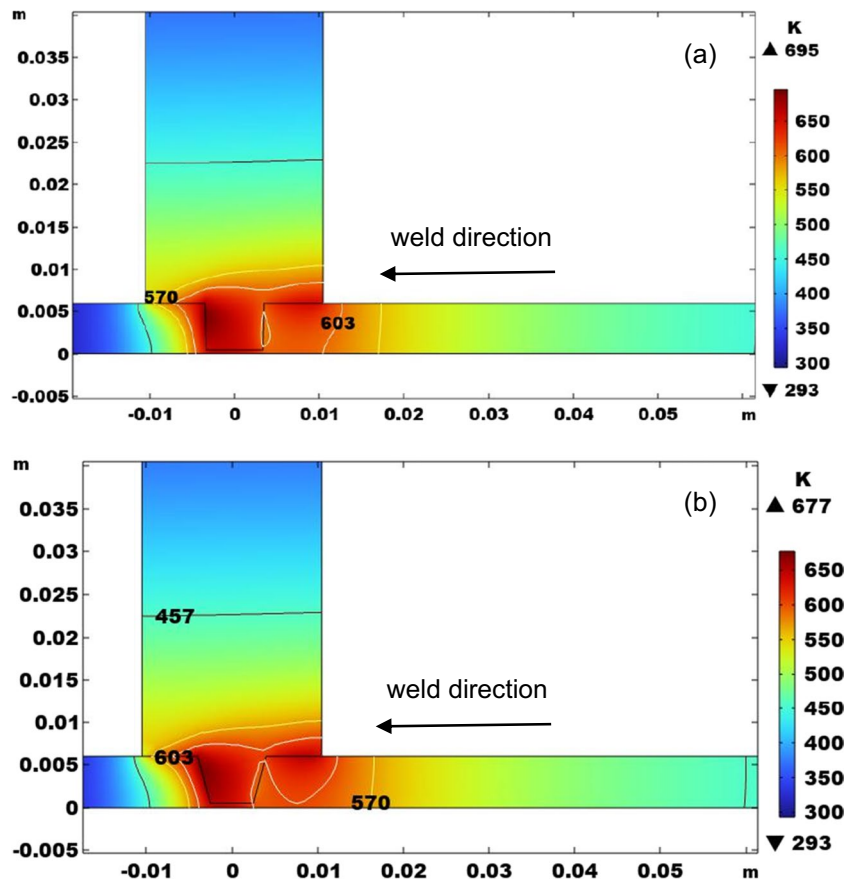


Fig. 8 Temperature distribution in workpiece materials, sectioned across the weld axis: **a** with cylindrical tool pin; **b** with conical tool pin

the present coupled model, and it requires a coupled Eulerian and Lagrangian (CEL) model.

3.2 Tool-pin profile effects on material flow and weldment zones

The objective of present numerical simulations is to study the effect of tool-pin profiles on thermal distribution, material flow, and mixing at higher traverse (welding) speed in friction stir butt welding of AA2219-T87 plates. The coupled

Eulerian model simulations of FSW process with two tool-pin profiles (cylindrical and conical) at fixed process parameters (traverse speed, 600 mm/min, and rotational speed, 750 rpm) are done, and the predicted results are discussed in terms of size and shape of weldment zones, thermal and material flow fields, shear strain rates, and thermal cycles. The key observations from the simulation results are discussed below.

Figures 5 and 6 show the evolution of temperatures within the workpieces due to moving heat source (cylindrical tool

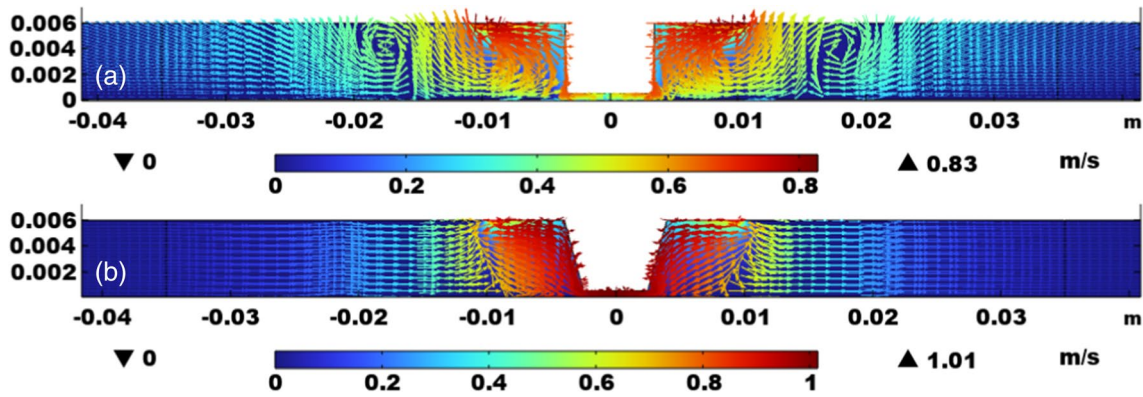
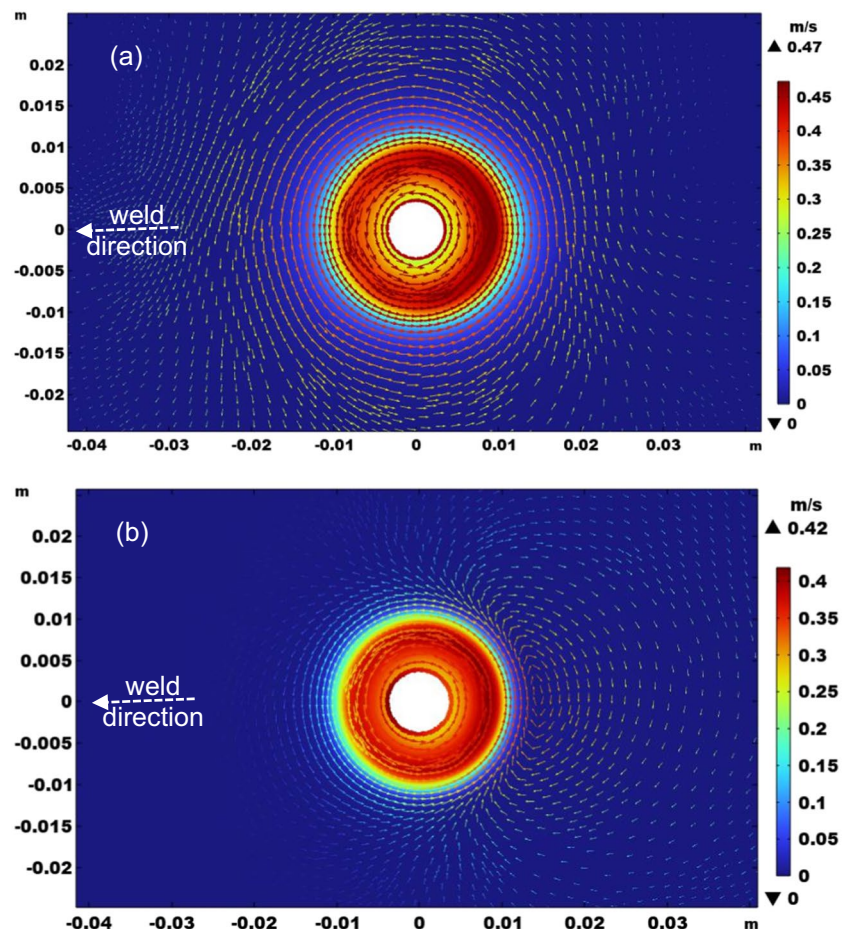


Fig. 9 Material flow velocity within the workpiece, sectioned across the weld axis: **a** with cylindrical tool pin; **b** with conical tool pin

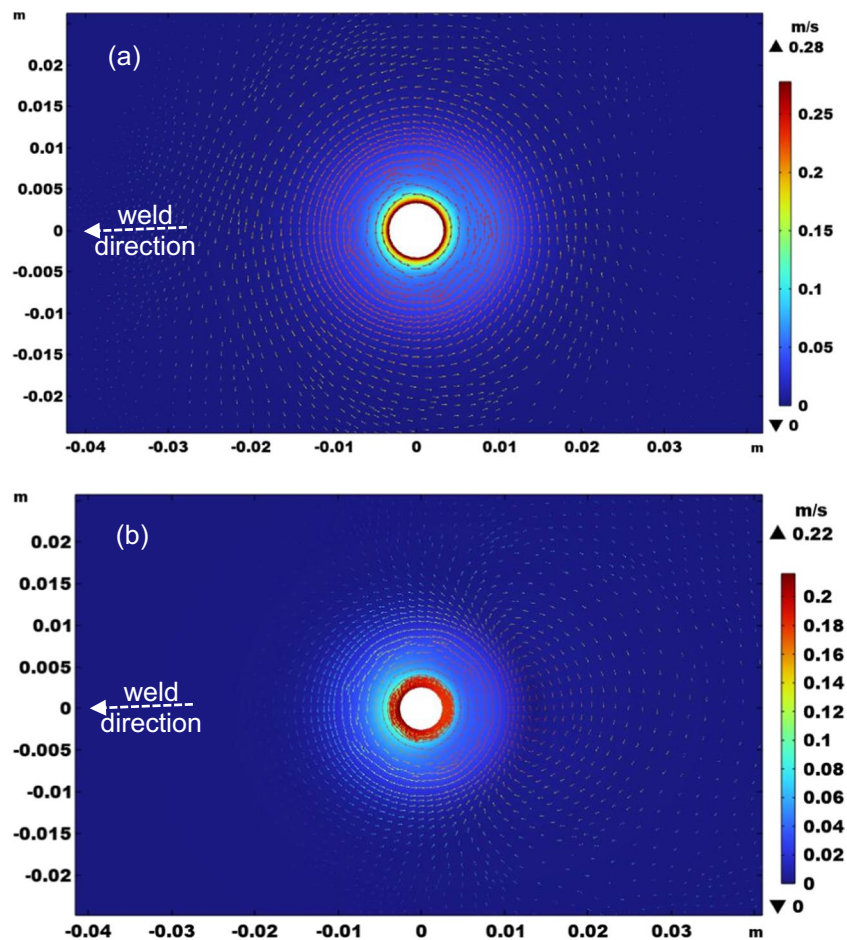
Fig. 10 Material flow velocity in the workpiece, sectioned at 1 mm below the top surface: **a** with cylindrical tool pin; **b** with conical tool pin



pin in Fig. 5 and conical tool pin in Fig. 6). As discussed in the model validation section, with increasing the simulation time, the temperatures increased everywhere within the workpieces. However, the increase in maximum temperature after 30 s is negligibly small and hence, the results after 60 s are considered steady state and used for a detailed comparison study on the effect of tool-pin profiles. It is found that

the maximum temperatures are with the cylindrical tool pin as compared to the conical tool pin, and it is due to increased frictional and shear deformation heat energy with the constant tool-pin radius. Figures 7 and 8 show the temperature distribution in workpiece and tool materials, sectioned along the weld axis (Fig. 7) and across the weld axis (Fig. 8), with two tool-pin profiles. It is observed that the maximum

Fig. 11 Material flow velocity in the workpiece, sectioned at 5 mm below the top surface: **a** with cylindrical tool pin; **b** with conical tool pin



temperatures are at the workpiece-tool interfaces (shoulder and pin surfaces), which is obvious because of frictional heat generation. Also, more heat is concentrated around the conical tool pin as compared to cylindrical tool pin, which means that the plasticized material flow with mixing around the conical tool pin is more than that of cylindrical tool pin. Further, the size of nugget zone (region above 45% of melting temperature, equals to isotherm of 603 K) is more with the cylindrical tool pin as compared to the conical tool pin (see Fig. 8), which means the possibility of more precipitate coarsening and grain growth, and both these phenomena would lower the weld joint strength with the cylindrical tool pin.

Figure 9 shows the predicted plasticized material flow due to shear by the rotating tool with cylindrical tool pin (Fig. 9a) and conical tool pin (Fig. 9b). It is interesting to observe that the maximum material flow velocity is with conical tool pin, and moreover, the velocities are higher around the conical tool pin as compared to cylindrical tool pin, which confirms that more heat energy is concentrated around the conical tool pin. This could be one possible reason why a conical tool pin gives defect-free weld as compared to cylindrical tool pin. The general fact with

FSW process is that more heat diffuses on the advancing side as compared to the retreating side, which results in high temperatures on the advancing side and less temperatures on the retreating side. Therefore, the material on the retreating side would be less plasticized as compared to that on the advancing side, and hence, the material follows the tool rotational direction (counter-clockwise), which is predicted by the present coupled thermal-material model. Further, the plasticized material flow region is slightly bigger on the advancing side as compared to that on the retreating side. To confirm further on the above-mentioned key observations, the predicted material flow pattern around the tool-pin profiles at two depths (1 and 5 mm) from the workpiece top surface is shown in Figs. 10 and 11. It is clearly observed that the material flow around the tool is counter-clockwise with decrease in flow velocity magnitudes across the tool-pin height. Also, due to fast heat diffusion on the head side (ahead of tool), the material flow velocities are low as compared to the tail side (behind the tool) with a vortex formation. Further, at a given depth, the material flow region with high velocities is found to be with conical tool pin as compared to cylindrical tool pin, which is in turn due to more energy being concentrated

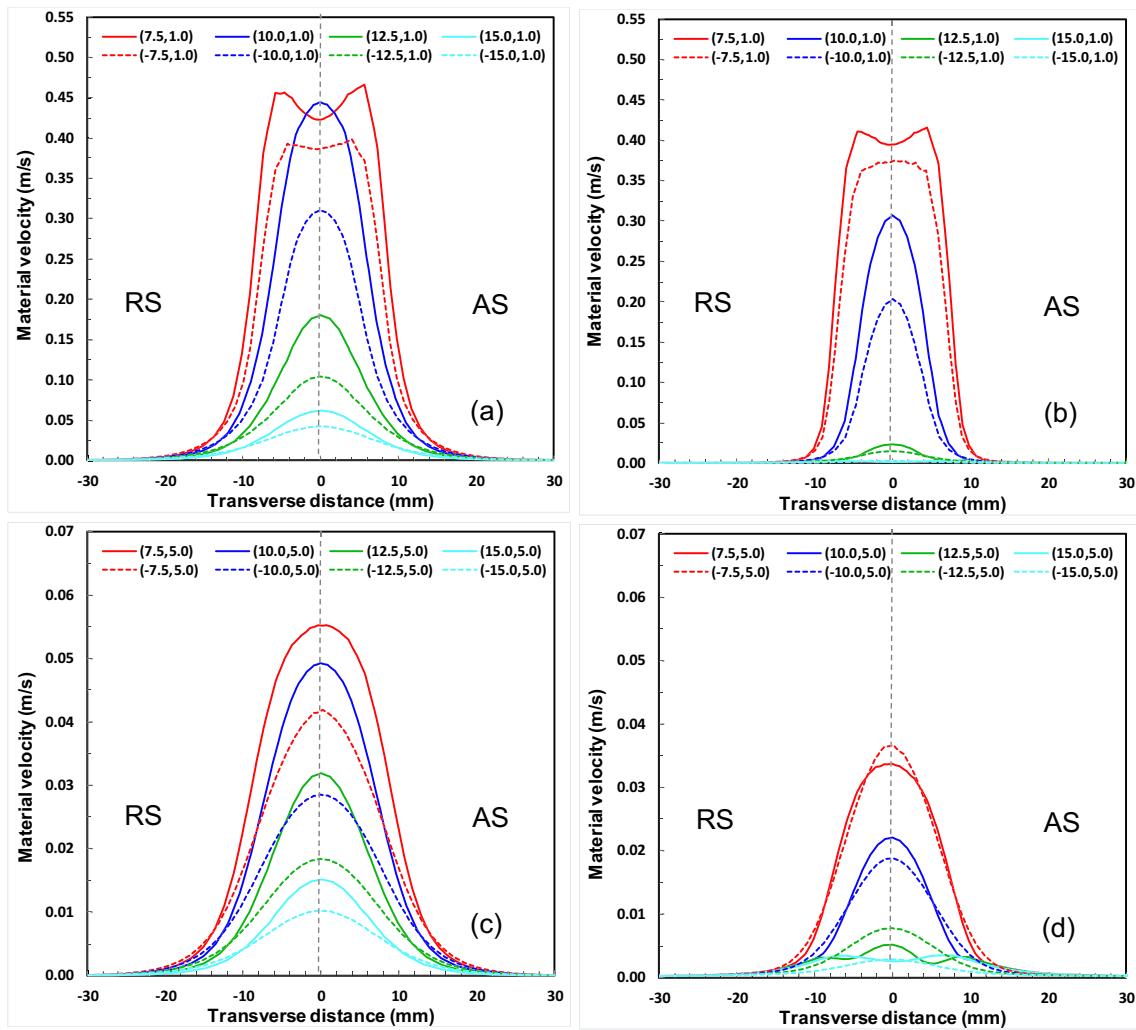


Fig. 12 Material flow velocity variation in transverse direction (head side: $x = -7.5, -10, -12.5, -15$ mm; tail side: $x = 7.5, 10, 12.5, 15$ mm) at two different depths ($z = 1, 5$ mm from top surface): **a, c** with cylindrical tool pin; **b, d** with conical tool pin

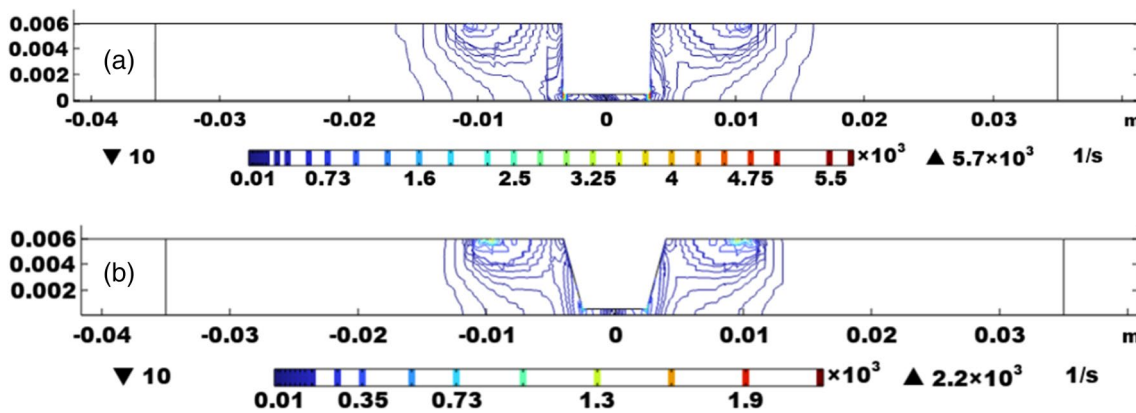


Fig. 13 Material shear strain rate variation around the tool, sectioned across the weld axis: **a** with cylindrical tool pin; **b** with conical tool pin

with the former case (as shown Fig. 9b). In order to study the tool-pin profile effect on the plasticized material flow and mixing, material flow velocity variation in the transverse direction is being studied at four locations away from the tool on head and tail sides and at two depths in the thickness direction, as shown in Fig. 12a and c. It is found that the velocity magnitudes are higher on the tail side as compared to the head side because more heat energy is accumulated on the tail side. Also, asymmetry in the material flow velocity on advancing and retreating sides is found, very close to the tool pin. Further, higher velocities are found with the cylindrical tool pin as compared to the conical tool pin (see Fig. 12b, d), which clearly demonstrates the coupled model prediction capability. Figure 13 shows the predicted shear strain rate ($\dot{\gamma}$) distribution in cross-sectional view and within the plasticized material flow with cylindrical tool pin (Fig. 13a) and conical tool pin (Fig. 13b). It can be clearly observed that the shear

strain rates are high near the shoulder outer edge as well as the tool-pin bottom edge, where the material is subjected to high temperatures and shear by the rotating tool. Further, the shear strain rates by the cylindrical tool pin are higher than those of the conical tool pin and are attributed to increased heat and shear because of the large radius of cylindrical tool pin. Further, to understand the shear strain rates around the rotating tool, a point-by-point variation in the transverse direction at four locations away from the tool on head and tail sides and at two depths from the workpiece top surface has been extracted and shown in Fig. 14. It can be clearly observed that the maximum shear strain rates are found to be on the tail side as compared to the head side and are attributed to more heat energy being accumulated on the tail side and less heat on the head side due to fast heat diffusion into the base material. Also, the shear strain rates decreased with the locations away from the tool, both on head and tail sides. Moreover, the shear

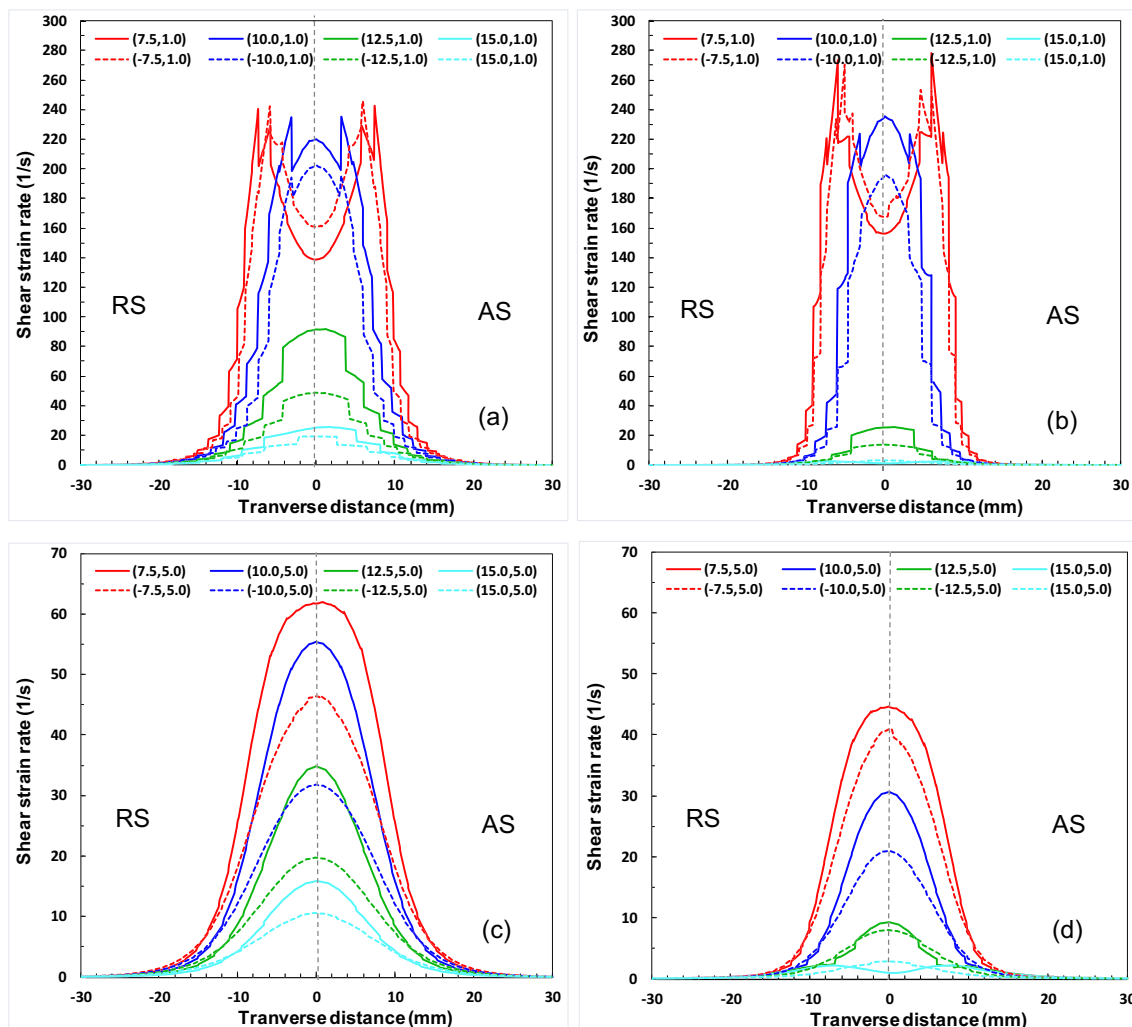


Fig. 14 Material shear strain rate variation in transverse direction (head side: $x = -7.5, -10, -12.5, -15$ mm; tail side: $x = 7.5, 10, 12.5, 15$ mm) at two different depths ($z = 1, 5$ mm from top surface): **a, c** with cylindrical tool pin; **b, d** with conical tool pin

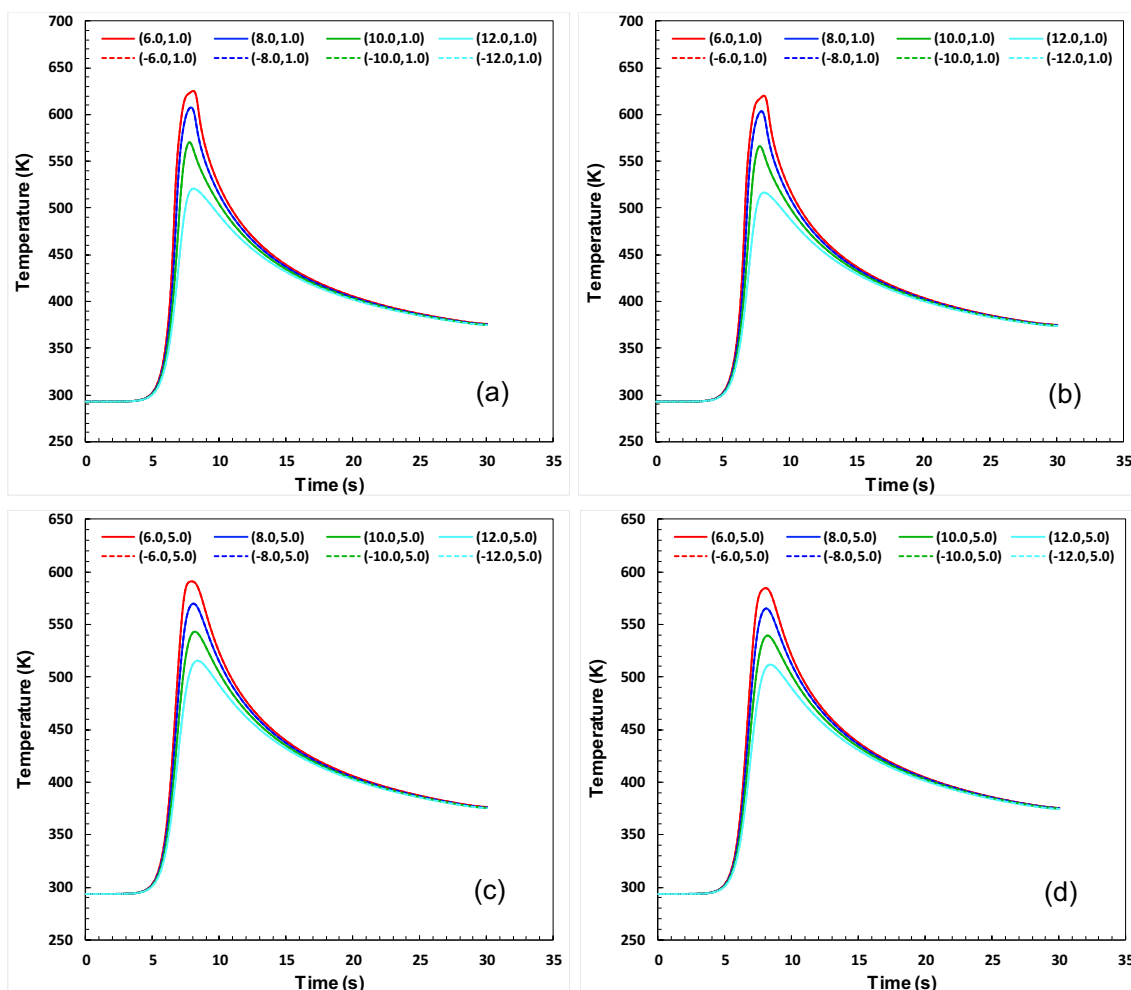


Fig. 15 Thermal cycles at four selected locations in transverse direction (retreating side, $y = -6, -8, -10, -12$ mm; advancing side, $y = 6, 8, 10, 12$ mm) at two depths ($z = 1$ and 5 mm from top surface): **a, c** with cylindrical tool pin; **b, d** with conical tool pin

strain rates with the cylindrical tool pin are high as compared to those of the conical tool pin and are attributed to increased heat and shear because of large radius with the former one.

In general, the macro- and micro-structures primarily depend on the thermal cycles (peak temperature, heating, and cooling rates) experienced by the workpiece material, which in turn depends on location from the centre of heat source. Figure 15 shows the predicted thermal cycles during the FSW process with the cylindrical tool pin (Fig. 15a, c) and conical tool pin (Fig. 15b, d) at four locations each on advancing and retreating sides and at two depths from the workpiece top surface. It can be observed that the peak (maximum) temperature, heating, and cooling rates are higher with the cylindrical tool pin as compared to the conical tool pin, and the magnitudes decreased with locations away from the tool axis. However, the difference in peak temperature, heating, and cooling rates on advancing and retreating sides was found to be negligibly small, and

it could be due to the absence of tool load and mechanical effects of workpiece material in the present coupled thermal-material flow model. Therefore, it can be stated that the higher temperatures with the cylindrical tool pin are due to increased frictional and deformation heat energy, which in turn affects the behaviour of θ -precipitates in aluminium alloy (AA2219-T87) and lowers the weld joint strength with the cylindrical tool pin as compared to the conical tool pin.

4 Summary

A coupled thermal-material flow (CFD) model has been developed and validated by comparing the predicted and measured weldment zones. Subsequently, the effect of tool-pin profiles (cylindrical and conical) in terms of the thermal and material flow fields and size of the weldment zones as well as the shear strain rate and thermal cycle variation on advancing and retreating sides of friction stir butt welds of

AA2219-T87 plates is studied. The key findings from the present numerical study are enumerated below:

- (i) Predicted size and shape of weld zones are in good agreement with the measured ones, which confirmed the coupled CFD model prediction accuracy.
- (ii) More heat is confined around the conical pin and resulted in higher material flow velocities around the tool, which would give defect-free welds as compared to cylindrical pin.
- (iii) At high traverse (welding) speed of 600 mm/min, the net heat input per unit length of the weld is low and results in smaller weld zones, which is predicted by the present coupled model—the size (width) of WNZ and TMAZ is smaller than the tool shoulder diameter.
- (iv) Shear strain rates are found to be more with the cylindrical pin as compared to the conical pin, which would result in grain elongation and lower the joint strength with the cylindrical tool pin.

Author contribution All authors contributed to the study conception and design. Model development, simulations, and analysis were done by Ramana Murthy Bagadi and Jeevan Jaidi. The first draft of the manuscript was written by Ramana Murthy Bagadi and Jeevan Jaidi and subsequently revised by Atmakur Venugopal Rao, and Suresh Dadulal Meshram. All authors read and approved the final manuscript.

Funding The present work was supported by the grant received from the Aeronautics Research and Development Board (AR&DB), Ministry of Science and Technology, Government of India (project no. ARDB/01/2032007/M/I).

Declarations

Conflict of interest The authors declare no competing interests.

References

1. Thomas WM, Nicholas ED, Needham JC, Murch MG, Temple-smith P (1991) Friction stir butt welding. International Patent Application No 5(460):317
2. Elangovan K, Balasubramanian V (2007) Influences of pin profile and rotational speed of the tool on the formation of friction stir processing zone in AA2219 aluminium alloy. *Mater Sci Eng A* 459:7–18. <https://doi.org/10.1016/j.msea.2006.12.124>
3. Elangovan K, Balasubramanian V (2008) Influences of tool pin profile and tool shoulder diameter on the formation of friction stir processing zone in AA6061 aluminium alloy. *Mater Des* 29:362–373. <https://doi.org/10.1016/j.matdes.2007.01.030>
4. Kumar K, Kailas SV (2008) The role of friction stir welding tool on material flow and weld formation. *Mater Sci Eng A* 485:367–374. <https://doi.org/10.1016/j.msea.2007.08.013>
5. Fratini L, Buffa G, Micari F, Shivpuri R (2009) On the material flow in FSW of T-joints: Influence of geometrical and technological parameters. *Int J Adv Manuf Technol* 44:570–578. <https://doi.org/10.1007/s00170-008-1836-3>
6. Biswas P, Mandal NR (2011) Effect of tool geometries on thermal history of FSW of AA1100. *Weld J* 90:129s–135s
7. Ramanjaneyulu K, Madhusudhan Reddy G, Venugopal Rao A, Markandeya R (2013) Structure-property correlation of AA2014 friction stir welds: role of tool pin profile. *J Mater Eng Perform* 22:2224–2240. <https://doi.org/10.1007/s11665-013-0512-4>
8. Ramanjaneyulu K, Madhusudhan Reddy G, Venugopal Rao A (2014) Role of tool shoulder diameter in friction stir welding: an analysis of the temperature and plastic deformation of AA 2014 aluminium alloy. *Trans Indian Inst Met* 67:769–780. <https://doi.org/10.1007/s12666-014-0401-z>
9. Meshram SD, Reddy GM, Rao AV (2016) Role of threaded tool pin profile and rotational speed on generation of defect free friction stir AA 2014 aluminium alloy welds. *Def Sci J* 66:57–63. <https://doi.org/10.14429/dsj.66.8566>
10. Meshram SD, Madhusudhan Reddy G (2018) Influence of tool tilt angle on material flow and defect generation in friction stir welding of AA2219. *Def Sci J* 68:512–518. <https://doi.org/10.14429/dsj.68.12027>
11. Xu S, Deng X, Reynolds AP, Seidel TU (2001) Finite element simulation of material flow in friction stir welding. *Sci Technol Weld Join* 6:191–193. <https://doi.org/10.1179/136217101101538640>
12. Schmidt H, Hattel J, Wert J (2004) An analytical model for the heat generation in friction stir welding. *Model Simul Mater Sci Eng* 12:143–157. <https://doi.org/10.1088/0965-0393/12/1/013>
13. Seidel TU, Reynolds AP (2001) Visualization of the material flow in AA2195 friction-stir welds using a marker insert technique. *Metall Mater Trans A* 32A:2879–2884. <https://doi.org/10.1007/s11661-001-1038-1>
14. Seidel TU, Reynolds AP (2003) Two-dimensional friction stir welding process model based on fluid mechanics. *Sci Technol Weld Join* 8:175–183. <https://doi.org/10.1179/136217103225010952>
15. Chen CM, Kovacevic R (2003) Finite element modeling of friction stir welding - thermal and thermomechanical analysis. *Int J Mach Tools Manuf* 43:1319–1326. [https://doi.org/10.1016/S0890-6955\(03\)00158-5](https://doi.org/10.1016/S0890-6955(03)00158-5)
16. Zhu XK, Chao YJ (2004) Numerical simulation of transient temperature and residual stresses in friction stir welding of 304L stainless steel. *J Mater Process Technol* 146:263–272. <https://doi.org/10.1016/j.jmatprotec.2003.10.025>
17. Chao YJ, Qi X, Tang W (2003) Heat transfer in friction stir welding - experimental and numerical studies. *J Manuf Sci Eng* 125:138–145. <https://doi.org/10.1115/1.1537741>
18. Zhang HW, Zhang Z, Chen JT (2005) The finite element simulation of the friction stir welding process. *Mater Sci Eng A* 403:340–348. <https://doi.org/10.1016/j.msea.2005.05.052>
19. Nandan R, Roy GG, Debroy T (2006) Numerical simulation of three-dimensional heat transfer and plastic flow during friction stir welding. *Metall Mater Trans A* 37A:1247–1259. <https://doi.org/10.1007/s11661-006-1076-9>
20. Nandan R, Roy GG, Lienert TJ, Debroy T (2006) Numerical modelling of 3D plastic flow and heat transfer during friction stir welding of stainless steel. *Sci Technol Weld Join* 11:526–537. <https://doi.org/10.1179/174329306X107692>
21. Buffa G, Hua J, Shivpuri R, Fratini L (2006) A continuum based fem model for friction stir welding - model development. *Mater Sci Eng A* 419:389–396. <https://doi.org/10.1016/j.msea.2005.09.040>
22. Buffa G, Hua J, Shivpuri R, Fratini L (2006) Design of the friction stir welding tool using the continuum based FEM model. *Mater Sci Eng A* 419:381–388. <https://doi.org/10.1016/j.msea.2005.09.041>

23. Khandkar MZH, Khan JA, Reynolds AP, Sutton MA (2006) Predicting residual thermal stresses in friction stir welded metals. *J Mater Process Technol* 174:195–203. <https://doi.org/10.1016/j.jmatprotec.2005.12.013>
24. Bastier A, Maitournam MH, Dang Van K, Roger F (2006) Steady state thermomechanical modelling of friction stir welding. *Sci Technol Weld Join* 11:278–288. <https://doi.org/10.1179/174329306X102093>
25. Grujicic M, He T, Arakere G et al (2010) Fully coupled thermo-mechanical finite element analysis of material evolution during friction-stir welding of AA5083. *Proc Inst Mech Eng Part B J Eng Manuf* 224:609–625. <https://doi.org/10.1243/09544054JEM1750>
26. Grujicic M, Pandurangan B, Yen CF, Cheeseman BA (2012) Modifications in the AA5083 Johnson-Cook material model for use in friction stir welding computational analyses. *J Mater Eng Perform* 21:2207–2217. <https://doi.org/10.1007/s11665-011-0118-7>
27. Grujicic M, Arakere G, Pandurangan B et al (2012) Computational analysis of material flow during friction stir welding of AA5059 aluminum alloys. *J Mater Eng Perform* 21:1824–1840. <https://doi.org/10.1007/s11665-011-0069-z>
28. Mohanty H, Mahapatra MM, Kumar P et al (2012) Study on the effect of tool profiles on temperature distribution and material flow characteristics in friction stir welding. *Proc Inst Mech Eng Part B J Eng Manuf* 226:1527–1535. <https://doi.org/10.1177/0954405412451811>
29. Al-Badour F, Merah N, Shuaib A, Bazoune A (2013) Coupled Eulerian Lagrangian finite element modeling of friction stir welding processes. *J Mater Process Technol* 213:1433–1439. <https://doi.org/10.1016/j.jmatprotec.2013.02.014>
30. Hamilton C, Kopysciański M, Senkov O, Dymek S (2013) A coupled thermal/material flow model of friction stir welding applied to Sc-modified aluminum alloys. *Metall Mater Trans A Phys Metall Mater Sci* 44:1730–1740. <https://doi.org/10.1007/s11661-012-1512-y>
31. Jain R, Pal SK, Singh SB (2016) A study on the variation of forces and temperature in a friction stir welding process: a finite element approach. *J Manuf Process* 23:278–286. <https://doi.org/10.1016/j.jmapro.2016.04.008>
32. Kadian AK, Biswas P (2017) Effect of tool pin profile on the material flow characteristics of AA6061. *J Manuf Process* 26:382–392. <https://doi.org/10.1016/j.jmapro.2017.03.005>
33. Sahlot P, Singh AK, Badheka VJ, Arora A (2019) Friction stir welding of copper: numerical modeling and validation. *Trans Indian Inst Met*. <https://doi.org/10.1007/s12666-019-01629-9>
34. Tiwari A, Pankaj P, Suman S, Biswas P (2020) CFD modelling of temperature distribution and material flow investigation during FSW of DH36 shipbuilding grade steel. *Trans Indian Inst Met* 73:2291–2307. <https://doi.org/10.1007/s12666-020-02030-7>
35. Pandian V, Kannan S (2020) Numerical prediction and experimental investigation of aerospace-grade dissimilar aluminium alloy by friction stir welding. *J Manuf Process* 54:99–108. <https://doi.org/10.1016/j.jmapro.2020.03.001>
36. Vicharapu B, Liu H, Fujii H et al (2020) Probing residual stresses in stationary shoulder friction stir welding process. *Int J Adv Manuf Technol* 106:1573–1586. <https://doi.org/10.1007/s00170-019-04570-9>
37. Kesharwani R, Imam M, Sarkar C (2021) Effect of flat probe on local heat generation and microstructural evolution in friction stir welding of 6061-T6 aluminium alloy. *Trans Indian Inst Met* 74:3185–3203. <https://doi.org/10.1007/s12666-021-02386-4>
38. Andrade DG, Leitão C, Dialami N et al (2021) Analysis of contact conditions and its influence on strain rate and temperature in friction stir welding. *Int J Mech Sci* 191:106095. <https://doi.org/10.1016/j.ijmecsci.2020.106095>
39. Su H, Wu CS, Bachmann M, Rethmeier M (2015) Numerical modeling for the effect of pin profiles on thermal and material flow characteristics in friction stir welding. *Mater Des* 77:114–125. <https://doi.org/10.1016/j.matdes.2015.04.012>
40. Shi L, Wu CS (2017) Transient model of heat transfer and material flow at different stages of friction stir welding process. *J Manuf Process* 25:323–339. <https://doi.org/10.1016/j.jmapro.2016.11.008>
41. Chen J, Shi L, Wu C, Jiang Y (2021) The effect of tool pin size and taper angle on the thermal process and plastic material flow in friction stir welding. *Int J Adv Manuf Tech* 116:2847–2860. <https://doi.org/10.1007/s00170-021-07650-x>
42. Jaidi J, Dutta P (2001) Modeling of transport phenomena in a gas metal arc welding process. *Numer Heat Transf Part A Appl* 40:543–562. <https://doi.org/10.1080/10407780152619838>
43. COMSOL Multiphysics (2015) Heat transfer module. © 1998–2018 Comsol 1–222. <https://doc.comsol.com/5.4/doc/com.comsol.help.heat/HeatTransferModuleUsersGuide.pdf>. Accessed May 2023
44. Schmidt HB, Hattel JH (2007) Thermal and material flow modelling of friction stir welding using COMSOL. Excerpt from the Proceedings of the COMSOL Conference Hannover. <https://www.comsol.com/paper/download/37785/Schmidt.pdf>. Accessed May 2023
45. Bachmann M, Carstensen J, Bergmann L et al (2017) Numerical simulation of thermally induced residual stresses in friction stir welding of aluminum alloy 2024-T3 at different welding speeds. *Int J Adv Manuf Technol* 91:1443–1452. <https://doi.org/10.1007/s00170-016-9793-8>
46. Colegrove PA, Shercliff HR (2004) Development of Trivex friction stir welding tool part 2 - three-dimensional flow modelling. *Sci Technol Weld Join* 9:352–361. <https://doi.org/10.1179/136217104225021661>
47. Li Q, Wu AP, Li YJ et al (2017) Segregation in fusion weld of 2219 aluminum alloy and its influence on mechanical properties of weld. *Trans Nonferrous Met Soc China (English Ed)* 27:258–271. [https://doi.org/10.1016/S1003-6326\(17\)60030-X](https://doi.org/10.1016/S1003-6326(17)60030-X)
48. Manikandan P, Prabhu TA, Manwatkar SK et al (2021) Tensile and fracture properties of aluminium alloy AA2219-T87 friction stir weld joints for aerospace applications. *Metall Mater Trans A Phys Metall Mater Sci* 52:3759–3776. <https://doi.org/10.1007/s11661-021-06337-y>
49. Kang J, Feng ZC, Frankel GS et al (2016) Friction stir welding of Al alloy 2219-T8: part I-evolution of precipitates and formation of abnormal Al₂Cu agglomerates. *Metall Mater Trans A* 47A:4553–4565. <https://doi.org/10.1007/s11661-016-3648-7>

Publisher's Note Springer Nature remains neutral with regard to jurisdictional claims in published maps and institutional affiliations.

Springer Nature or its licensor (e.g. a society or other partner) holds exclusive rights to this article under a publishing agreement with the author(s) or other rightsholder(s); author self-archiving of the accepted manuscript version of this article is solely governed by the terms of such publishing agreement and applicable law.